Full length article

In vitro evaluation of stress corrosion cracking susceptibility of PEO-coated rare-earth magnesium alloy WE43

Julia Nachtsheim [a], Songyun Ma [a,*], Jaka Burja [b,c], Bernd Markert [a]

[a] *Institute of General Mechanics, RWTH Aachen University, Eilfschornsteinstraße 18, 52062 Aachen, Germany*
[b] *Institute of Metals and Technology, Lepi pot 11, 1000 Ljubljana, Slovenia*
[c] *Department of Materials and Metallurgy, Faculty of Natural Sciences and Engineering, University of Ljubljana, Aškerčeva cesta 12, 1000 Ljubljana, Slovenia*

A B S T R A C T

Controlling material degradation in complex mechanobiological environments is the current challenge in advancing biodegradable magnesium implants for orthopaedic applications. Understanding stress corrosion cracking (SCC) mechanisms of magnesium alloy-coating systems in physiological fluids facilitates the design of magnesium implants with excellent biomedical performance. In this study, we investigated the SCC behaviour of a medical grade PEO-coated magnesium alloy WE43 under different loading conditions. Constant loadings tests (CLT) and slow strain rate tests (SSRT) were conducted to evaluate the SCC susceptibility of this alloy-coating system under in vitro conditions. Fracture surfaces of the non-coated and PEO-coated specimens were characterised by scanning electron microscopy to reveal the SCC mechanisms under different loading configurations. The experimental results showed that the alloy-coating system exhibits a high SCC resistance in SSRT conditions. However, high stress levels and plastic deformations lead to a significant acceleration of the SCC process. Moreover, the fracture surface analysis demonstrated that the brittle nature of the PEO coating deteriorates the mechanical integrity of the alloy under critical mechanical loadings, which results in an increased susceptibility towards stress corrosion cracking of the coated WE43.

1. Introduction

For developing innovative temporary metallic implants, biodegradable magnesium alloys have been applied in next-generation orthopaedic implants [1–4], possessing excellent mechanical properties, good biocompatibility and biosafety. The inconsistent mechanical properties between bone tissues and conventional implant materials can lead to undesired stress-shielding effects, resulting in pathological changes in the surrounding healthy bone tissue [5]. Magnesium alloys considerably reduce stress-shielding risk due to their similar mechanical properties to native bone tissue [6,7]. Furthermore, magnesium implants can naturally degrade in the human body and do not need to be removed in a second surgery. Recently, biocompatible coatings like plasma electrolytic oxidation have been successfully introduced to improve the corrosion resistance of orthopaedic implants significantly [8,9]. In this context, various studies have reported the positive effect of the PEO coating to enhance osseous integration and increase bone density at the implant interface [10,11].

Biodegradable orthopaedic implants, exposed to the aggressive physiological corrosion environment and considerable mechanical loadings, need to be designed to support the fractured bone throughout the entire healing process. The interactions of mechanochemical loadings can lead to a drastic loss of mechanical integrity due to stress corrosion cracking (SCC). Slow and sub-critical crack growths until final material failure in the SCC process are accompanied by a significant loss of ductility [12,13]. In general, the susceptibility of magnesium alloys towards SCC is related to the general corrosion resistance, the vulnerability towards pitting corrosion, hydrogen embrittlement or anodic dissolution. Furthermore, SCC susceptibility strongly depends on the corrosion environment. High chloride concentrations have been reported to lead to more pronounced pitting corrosion and facilitate hydrogen embrittlement [14]. Moreover, corrosion pits are identified as the main precursor of SCC initiation as they cause local stress concentrations [15,16]. Therefore, the alloy's pit corrosion resistance plays an important role in the susceptibility towards SCC [17].

Recently, considerable research efforts have been devoted to linking the microstructure of magnesium alloys with the SCC behaviour. It is reported that aligned secondary phases serve as preferentially crack

---

* Corresponding author.
E-mail address: ma@iam.rwth-aachen.de (S. Ma).

propagation paths and thereby increase the SCC susceptibility of an Mg—Mn alloy [18]. Alloys with very or ultrafine grain (~ 1–2 μm) exhibit excellent mechanic properties and corrosion resistance [14,19,20]. Grain refinement (~ 3–8 μm) has been shown to increase the SCC resistance of ME21 and AZ31B alloy [21,22]. The improvement is attributed to the higher proportion of grain boundaries after refinement, which results in improved protection of the oxide film and high-density crystal defects that promote the passivation process. Furthermore, it is reported that a wider nanocrystalline layer in a compressive stress state in the near-surface region achieved by cryogenic cooling can significantly improve the SCC resistance of an AZ31 alloy in SBF [23].

In addition to microstructural modification and optimisation, surface coatings are another powerful approach to tailor the corrosion behaviour of magnesium alloys. Nonetheless, the efficiency of the surface coatings to improve SCC resistance under mechano-chemical loadings is still an open issue, as the brittle nature of such coatings can also negatively affect the mechanical integrity of the alloy-coating system. Due to its low fracture toughness, cracks easily initiate in coatings and propagate into the substrate, inducing local stress concentrations and facilitating the initiation of SCC in alloy substrates. In-situ SSRT experiments in air have revealed that cracks initiate at thickened coating sites of the coating-substrate interface and subsequently propagate into the metallic substrate [24]. It was shown that thicker coatings facilitate crack initiation [24]. Cracking of the PEO coating instead of corrosion pits was observed as the driving factor for SCC in slow strain rate tests (SSRT) of magnesium alloy AM50 in an unphysiological fluid [25]. The latest progress has been made in developing self-healing coatings to mend defects that occur due to the brittle nature of the coating. An LSP/MAO composite coating was found to significantly improve the SCC performance of AZ80 alloy in SBF, which was attributed to the coating's self-healing mechanism to form a dense passive film at emerging damaged spots between LSP and MAO layers during SSRT [26]. It is generally accepted that the innermost dense barrier layer determines the coating's efficiency towards corrosion resistance. However, the correlation between these critical coating features and the SCC resistance has not been assessed quantitatively.

To characterise the SCC behaviour of magnesium alloy-coating system, the choice of corrosion media plays a critical role in in vitro experiments [27–31] and relevant bioorganic components significantly affect corrosion [31–34]. However, using complex solutions involves certain limitations due to the fluid's vulnerability to microbial development and the high requirements of sterile experimental conditions. As a result, numerous studies of SCC experiments were performed in inorganic chloride solutions without accounting for the effects of organic compounds [18]. The risk of contamination by using organic fluids was emphasised by Chen et al. [35]. They assessed the influence of organic fluid compounds on the SCC susceptibility of an Mg—1Zn alloy in non-sterile conditions. It was confirmed that the inorganic-organic hybrid corrosion product film retards the crack initiation and increases the SCC resistance. Moreover, the protein bovine serum albumin (BSA) was found to temporarily protect the aluminium-containing magnesium alloy AZ91D in a physiological solution, since initial surface adsorption of the protein leads to the chelation of the protein with the corrosion product [36]. Therefore, it is crucial to investigate the SCC behaviour of magnesium alloy-coating systems in physiological organic solutions for a reliable design of biodegradable magnesium implants.

Addressing the related critical issues in the application of complex organic fluids, we developed a test bench for performing in vitro corrosion experiments under mechanical loadings in sterile conditions. In this study, the designed experimental setup is used to evaluate the influence of a plasma-electrolytic (PEO) coating on the SCC susceptibility of a rare-earth magnesium alloy WE43 with very fine grain sizes. WE43 magnesium alloy is considered as one of the most promising magnesium alloys for biodegradable orthopaedic implants and stents, due to its good biocompatibility, biosafety and corrosion resistance [11,37]. Furthermore, WE43 is alloyed with rare-earth elements and

does not contain aluminium, which is linked to Alzheimer's disease and cancer [38,39]. The used complex cell culture medium Dulbecco's Modified Eagle's Medium (DMEM) contains bio-relevant compounds, e. g., amino acids, glucose and vitamins. As shown in a previous study of our research group, the PEO coating provides long-term protection and efficiently preserves the mechanical integrity of WE43 in in vitro experiments without mechanical loading [40]. In this work, we systemically studied the effect of external loadings on the SCC behaviour of the non-coated and PEO-coated WE43. To this end, the SCC susceptibility was evaluated by constant loading tests (CLT) with three different stress levels and slow strain rate tests (SSRT) with three different strain rates. In the CLT tests, the degradation of the material integrity was subsequently quantified by tensile tests. To reveal the SCC mechanism under different loading configurations, fracture surfaces of the non-coated and PEO-coated specimens were carefully analysed by scanning electron microscopy.

2. Experimental setup for in vitro corrosion experiments

The newly developed experimental setup enables corrosion experiments under mechanical loadings in aseptic and temperature-regulated conditions. The specimen is mounted in its individual and enclosed corrosion cell that retains sterile conditions outside sterile laboratory devices. On this account, all parts can be sterilised and assembled inside a clean bench class 100 equipped with a HEPA-filter. The test setup is designed in a modular manner, and three specimens can be tested in series within an integrated test bench under mechanical loadings in the horizontal direction. The cell is composed of three main parts, as shown in Fig. 1: A glass bottle, a central transparent cube, and a lid.

The cube is manufactured from solid acrylic glass, a translucent material enabling visual control of the pH indicator of the corrosion fluid. The radial seal shafts are designed to fit the shoulders of the specimen. The transparent cube is connected to a wide-neck bottle for providing a sufficient corrosion fluid volume. The lid of the cell allows gas exchange via filtering caps that are commonly used for cell culture flasks. After assembly of the corrosion cell in sterile conditions, the enclosed corrosion cell is integrated into the test bench. The test bench is controlled by FlexTest 60 (MTS Systems Corp., Minneapolis, USA) and equipped with a force transducer (Model 661.20F-03, MTS Systems Corp., Minneapolis, USA). A tempering unit provides constant temperature of 37° ± 1 °C. Finally, a magnetic stirrer is placed underneath the glass bottle that gently stimulates the magnetic stirrer inside the fluid.

3. Materials and methods

3.1. Magnesium alloy and PEO coating

Round tensile test specimens were manufactured from as-extruded WE43 magnesium alloy rods and provided by Medical Magnesium GmbH (Aachen, Germany). According to DIN 50125, tensile test specimens were designed with a diameter of 4 mm to fit the dimensions of the corrosion cell for ensuring sealing functionality, as shown in Fig. 2. Table 1 shows the chemical composition of the alloy measured by inductively coupled plasma atomic emission spectroscopy (Varian 720-ES, Agilent Technologies, CA, USA). For the microstructural analysis, specimens were cut perpendicular to the direction of extrusion, mounted in epoxy resin, ground and polished, then etched with 2 % nital and sputtered with carbon. The PEO surface modification was conducted in a constantly cooled phosphate-based electrolyte at a regulated temperature between 20 °C and 34 °C with a bi-polarly pulsed rectifier set, and tensile specimens were constantly rotated for achieving a homogeneous coating thickness. Process parameters were chosen to generate a coating of 19 ± 5 μm thickness with interconnected and isolated pores of up to 3–5 μm as shown in Fig. 3. A more detailed description and analysis of the generated coating is presented in [40].
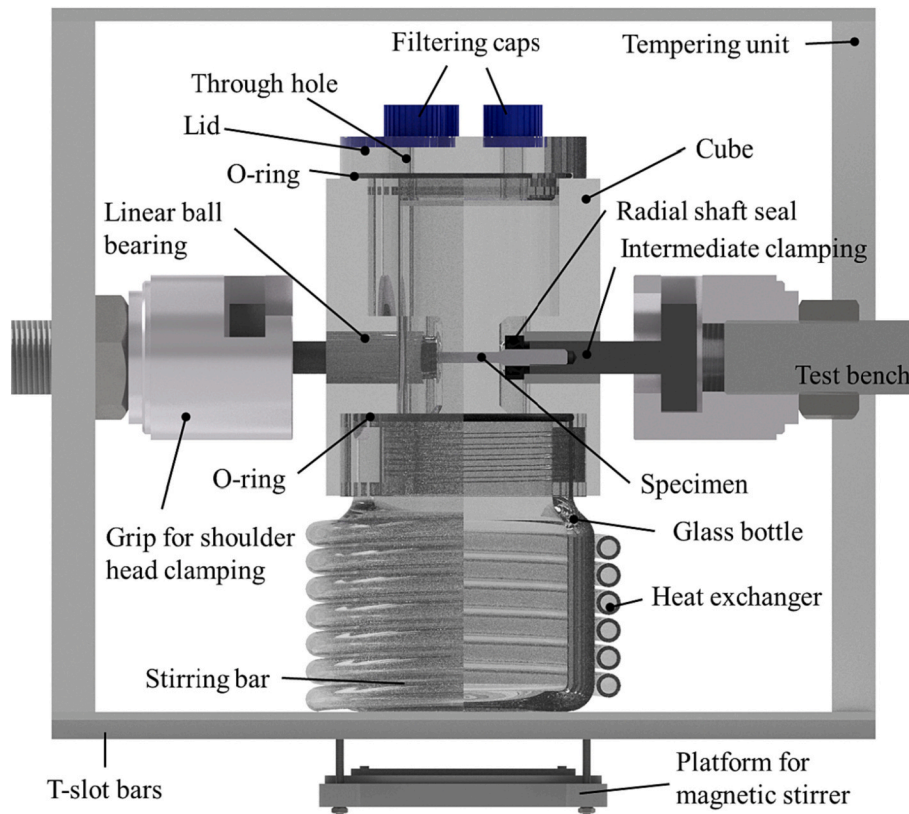
Fig. 1. Corrosion cell mounted on a test bench inside a tempering unit for investigating the SCC behaviour of magnesium alloys under in vitro conditions.
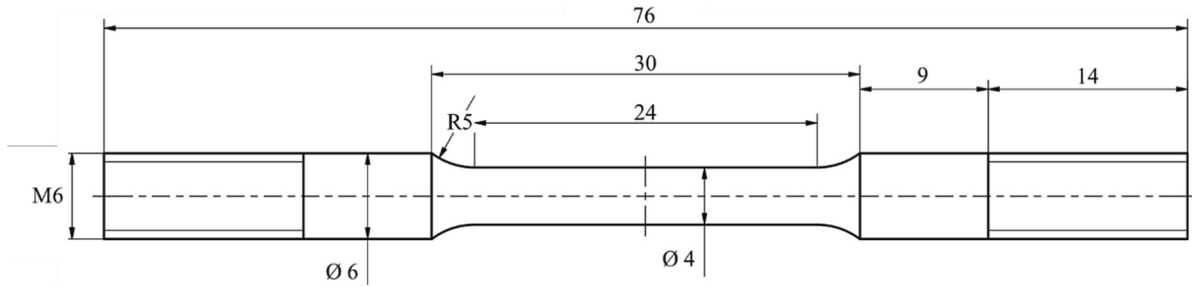
Fig. 2. Dimensions of tensile specimens used for in vitro experiments; Dimensions given in mm.

Table 1
Chemical composition of WE43 in wt%.

Y	Nd	Zr	Al	Mn	Fe	Mg
3.8	2.6	0.02	< 0.01	0.0025	0.0065	Bal.

3.2. Corrosion medium

650 mL of the cell culture medium Dulbecco's Modified Eagle's solution (DMEM, L0101–500, Biowest, Nuaillé, France) supplemented with 5 mL Penicillin-Streptomycin (ThermoFisher Scientific Inc., Waltham, MA, USA) and 5 mL Amphotericin B (ThermoFisher Scientific Inc., Waltham, MA, USA) was used for corrosion experiments. The chosen fluid volume considers the suggestions on the ratio between fluid volume and sample surface area. The composition of the DMEM is presented in [41] and its ionic concentration is compared to the ionic concentration of human blood plasma in Table 2.

3.3. Constant loading test

CLT tests were performed with stress levels below the material's yield strength, which are 80 %, 60 %, and 40 % of the materials' initial tensile strength R_m. In the CLT tests, the specimens were loaded by a controlled force. The target force was held constantly for the entire test period of either 1 day or 3 days to investigate the stress corrosion behaviour. We selected the stress corrosion period of 3 days for comparison with the experimental studies of biodegradable magnesium alloys in [42,43]. The shorter 1 day test period was motivated by the results of our previous study, which reveals the highest corrosion rate of WE43 alloy in immersion tests during the initial 24 h [40]. The target force was derived from the initial specimen diameter and the chosen stress levels. Hence, the engineering stress was considered in the experiments. To consider statistical differences in substrate and coating properties, three specimens were tested for each specimen group and stress level. Subsequently, mechanical degradation during the CLT test was analysed by tensile tests.

After mounting specimens into the corrosion cell in sterile conditions, the cell was integrated into the test bench. The corrosion cell was
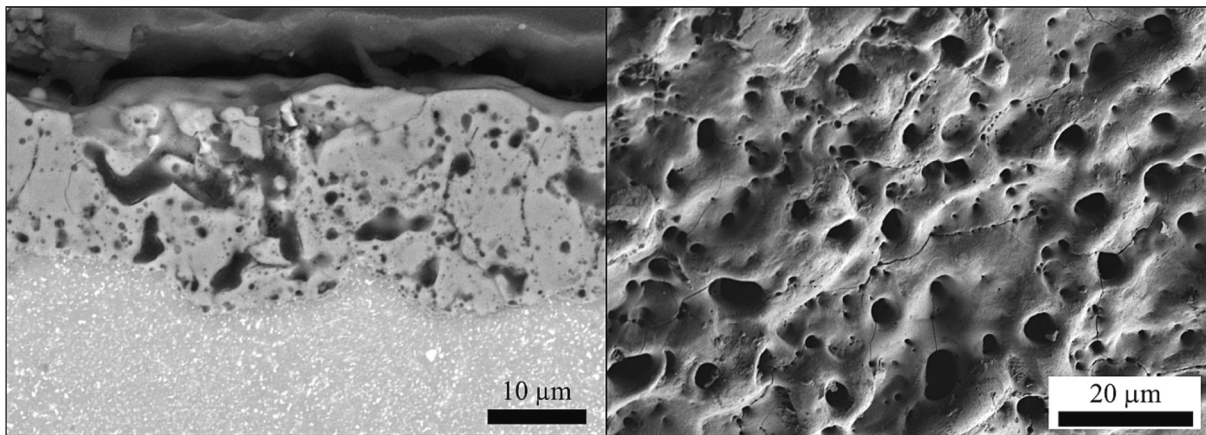
Fig. 3. BSE SEM image of the coating substrate interface (left). SEM image of the coating surface (right).

Table 2
Ionic concentrations in mmol/L.

Ion	Na^+	K^+	Mg^{2+}	Ca^{2+}	Cl^-	HCO_3^-	HPO_4^{2-}	SO_4^{2-}
Blood Plasma	142	5	1.5	2.5	103	27	1	0.5
DMEM	154	5.4	0.8	1.8	119	44	1	0.8

topped up with test solution, and specimens were directly loaded. The target load was applied at a rate of 40 N/s. After the test period, specimens were removed from the corrosion cell, rinsed with distilled water and ethanol, dried and tensile tested.

3.4. Tensile tests

Tensile tests were performed on a MTS Minibionix II testing machine (MTS Systems GmbH, Germany) at a displacement rate of 1 mm/min. The strain of specimens was measured by GOM Aramis SRX Adjustable (Carl Zeiss GOM Metrology GmbH, Germany). Experimental data was processed in MATLAB, and material properties were calculated according to ISO 6892-1:2016.

3.5. Slow strain rate test

SSRT experiments were performed with three different strain rates, and three specimens were used for each strain rate. The specimens were continuously strained to failure, and the total tensile force on the specimens was measured by the force sensor of the tensile machine. The largest actuator speed of 5.2 µm/min corresponds to a strain rate of 1.1 $10^{-6}\,s^{-1}$ (referred to as v1) in the elastic regime. Additionally, tests were performed with slower speeds 1.7 µm/min (referred to as v2) and 1.0 µm/min (referred to as v3) to assess the influence of the strain rate. As no extensometer was attached to the specimen's gauge length in corrosion conditions, the strain in SSRT tests is calculated from the calibrated relation between the measured tensile strain and displacement in air. After testing, specimens were rinsed with distilled water and ethanol. For evaluating the SCC resistance of the alloy systems, the SCC susceptibility indices I_{UTS} and I_ε were calculated for the tensile strength and the elongation-to-failure with respect to the uncoated WE43 specimens using [17]:

$$I_{UTS} = \left(UTS_{air} - UTS_{fluid} \right) \big/ UTS_{air} * 100\% \tag{1}$$

$$I_\varepsilon = \left(\varepsilon_{f-air} - \varepsilon_{f-fluid} \right) \big/ \varepsilon_{f-air} * 100\% \tag{2}$$

3.6. Scanning electron microscopy and transmission electron microscopy

Scanning electron microscopy was used for fractography and microstructural analysis of etched WE43 using a FIB-SEM Zeiss Cross-Beam 550. Samples for transmission electron microscopy (TEM) were prepared using argon ion-slicing with JEOL EM-09100IS Ion Slicer and observed with TEM (JOEL JEM-2100).

4. Results and discussion

4.1. Microstructure

Fig. 4 shows the alpha magnesium matrix with intermetallic precipitates. The average grain size diameter measured using the intercept method is 2.7 µm. The precipitates are small, <0.1 µm in diameter, which makes the EDS analysis less accurate as the analysis volume is relatively large, but it can be regarded as an indicator. The small intermetallic precipitates in WE43 alloy are Mg-Y-Nd intermetallic phases, as confirmed by EDS analysis. The secondary Mg-Y-Nd precipitates are typically β ($Mg_{14}YNd_2$) and $β_1$ ($Mg_3(Y,Nd)$).

4.2. Constant loading testing

Fig. 5 shows the residual tensile strength determined by tensile tests after corrosion in DMEM for one or three days with three different stress levels: 40 %, 60 % and 80 % of the material's initial tensile strength R_m. The material shows an excellent combination of high tensile strength and ductility in the extruded WE43 alloy with fine grain sizes. The alloy's tensile strength of about 300 MPa is quite high in comparison with other comparable WE43 alloys tested in [17,43]. The initial tensile strength of the PEO-coated alloy is marginally lower (approx. 2 %), which can be attributed to either the small reduction in the diameter of substrate material due to the coating process or the brittle coating facilitating the formation of crack initiation sites. The SCC experiment results under constant loadings reveal a critical stress level of 0.8 R_m, leading to a high probability of specimen failure during the first 24 h in both uncoated and coated specimen groups. In both specimen groups, two out of three specimens failed. In experiments with stress levels below the critical value of 0.8 R_m, the residual tensile strength only decreased slightly independent of the stress level and loading duration. The reduction measured for the uncoated specimens was between 2.1 and 3.4 %, whereas the reductions of the coated specimen groups were slightly smaller, accounting for values between 1.4 and 2.2 %. Interestingly, the residual tensile strength of the specimens that did not fail in the CLT tests with the critical stress level of 0.8 R_m is comparable to the residual strength of the specimens after CLT tests with lower stress levels. A comparable minor decrease in the ultimate strength of about 3
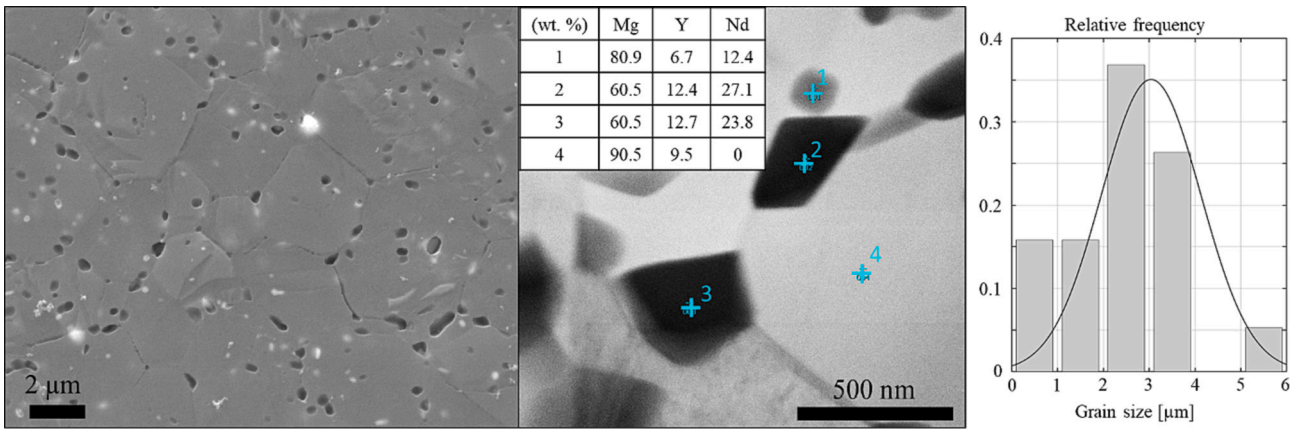
Fig. 4. SEM image of etched WE43 alloy with marked grain boundaries (left), and TEM image of the magnesium alloy with EDS measurements (middle), and grain size distribution (right).
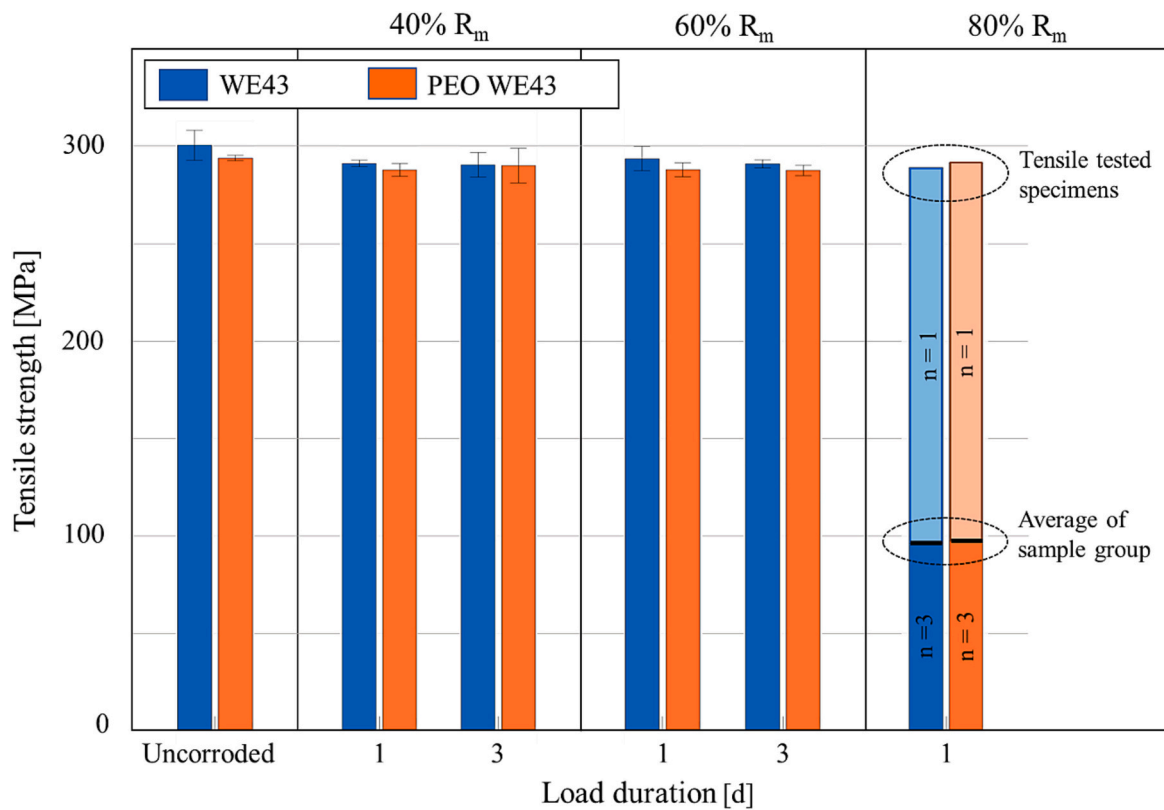
Fig. 5. The residual tensile strength of non-coated (blue) and PEO-coated (red) WE43 specimens after constant loading tests with varying stress levels for 1 and 3 days loading durations.

% after 3 days in CLT conditions in SBF was also observed by Wang et al. [43]. In their experiments, specimens were exposed to significantly smaller stress levels of up to 38 % of the initial material strength, and a minor decrease in material strength was reported independently of the stress level. A magnesium alloy ZK40–0.4Sr tested in m-SBF with a stress level of 0.08 R_m for 3 days showed a decrease in strength of about 5 %, while the tensile strength of the PEO-coated magnesium alloy did not change [42].

The fracture of the uncoated alloy is of ductile nature, as shown in Fig. 6a. In contrast, Fig. 6b shows the coated fracture surface with smooth and brittle fracture regions close to the circumference and ductile regions in the centre with dimple formation. The SEM fracture surface of the coated specimen indicates crack initiation sites inside the brittle coating. Fig. 6c and Fig. 6d reveal a large number of secondary cracks that propagate into the substrate material. This observation confirms the feature of crack initiation of PEO-coated alloys in air reported in [24]. The initiation site has been linked to the irregular interface between coating and alloy substrate and preferentially occurs at thicker coating spots [44]. The brittle nature of the coating changes the overall fracture morphology.

The fracture surface of an uncoated specimen that failed after 7 h loaded with the largest stress level of 0.8 Rm is shown in Fig. 7. Crack growth mechanisms of stress-assisted cracking are clearly identified in the fracture surface. After crack initiation, the crack slowly progresses and allows fluid to access the crack surfaces which in turn leads to additional material degradation caused by corrosion and hydrogen-
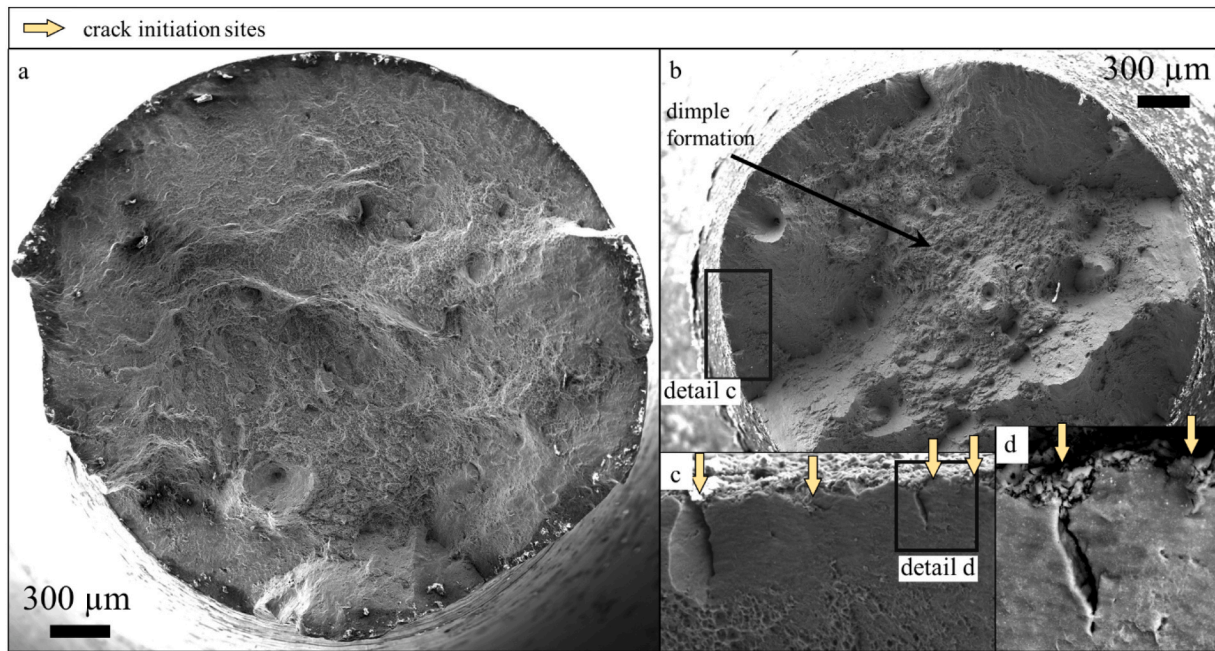
Fig. 6. SEM image of the fracture surfaces of specimens tested in air: (a) Ductile fracture features of uncoated specimen. (b) A combination of ductile and brittle fracture features of coated specimen. (c) Crack initiation inside the coating in region c. (d) Higher magnification of a crack initiation side propagating from the coating into the substrate material.
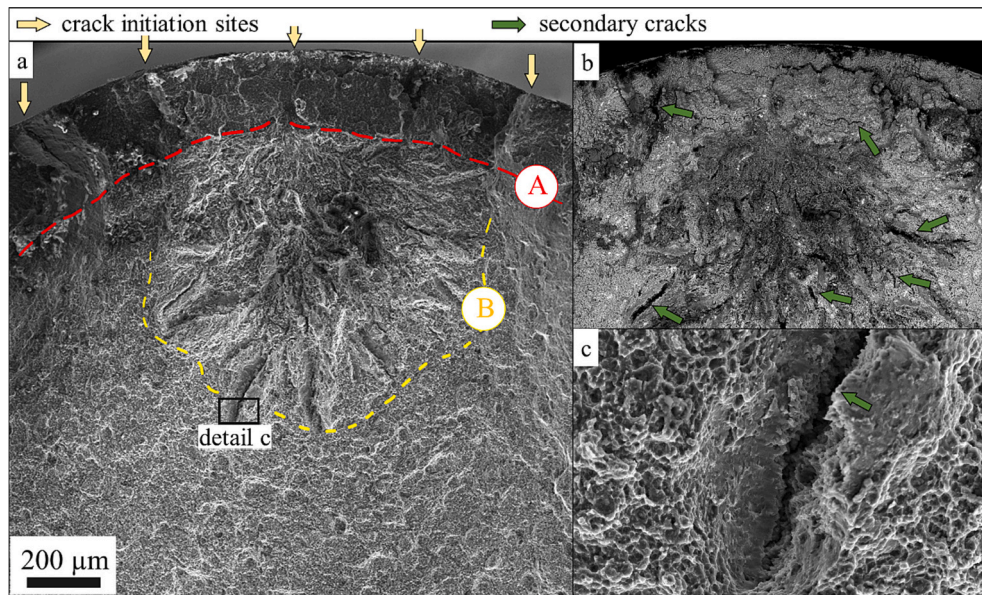
Fig. 7. SEM image of the fractured uncoated WE43 alloy in the 0.8 R_m CLT test: (a) Stress corrosion cracking in area A and brittle fracture features in area B with steep ridges. (b) BSE SEM image revealing oxidations and secondary cracks in areas A and B. (c) Detail of secondary cracks in the brittle fracture zone.

assisted mechanisms [45]. It is seen that the synergy between corrosion and crack propagation leads to a distinct circumferential region of stress corrosion cracking in the fracture surfaces (marked area A), which has been well reported for aluminium-free magnesium alloys [35,45,46]. For uncoated magnesium alloys, the size of this area has been related to the alloy's SCC resistance. A thicker area indicates better SCC resistance as the material has been longer exposed to the external load inside the corrosion environment [20,45]. The fracture surface of a coated specimen failing after 9.7 h in the test with a stress level of 0.8 R_m is shown in Fig. 8. Compared with the uncoated specimen, the area of stress corrosion cracking (area A) is smaller, implying that the coated specimen is more susceptible to SCC. Nevertheless, the residual yield strength after

CLT tests (see Fig. 5) shows no differences in SCC susceptibility between coated and non-coated specimens. It is indicated that the coating not only turns the SCC failure mechanism of magnesium alloys but also crack growth rates at different stages of SCC. Furthermore, both fracture surfaces show brittle fracture patterns adjacent to the region of stress corrosion cracking, and the SEM images reveal oxidations inside this region, as shown in Fig. 7b and Fig. 8b.

As illustrated in Fig. 9, the precursor event of SCC is corrosion pits that locally increase the stress concentration at an early experimental stage. In contrast, the PEO coating protects the underlying substrate from corrosion attack at this stage. Van Gaalen et al. [47] reported that the PEO coating on WE43 alloy not only significantly retards the
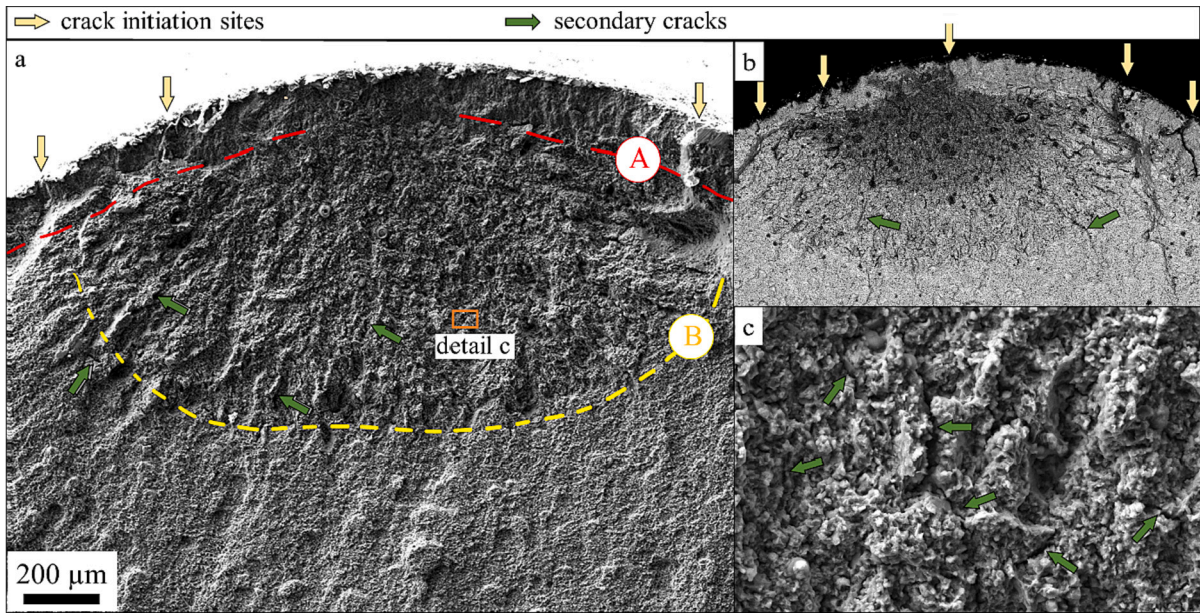
Fig. 8. SEM image of the fractured coated WE43 specimen in the 0.8 R_m CLT test: (a) Stress corrosion cracking inside a smaller area A and brittle fracture features in area B of smooth appearance. (b) BSE SEM image revealing oxidations and secondary cracks. (c) Detail showing a larger number of smaller secondary cracks.
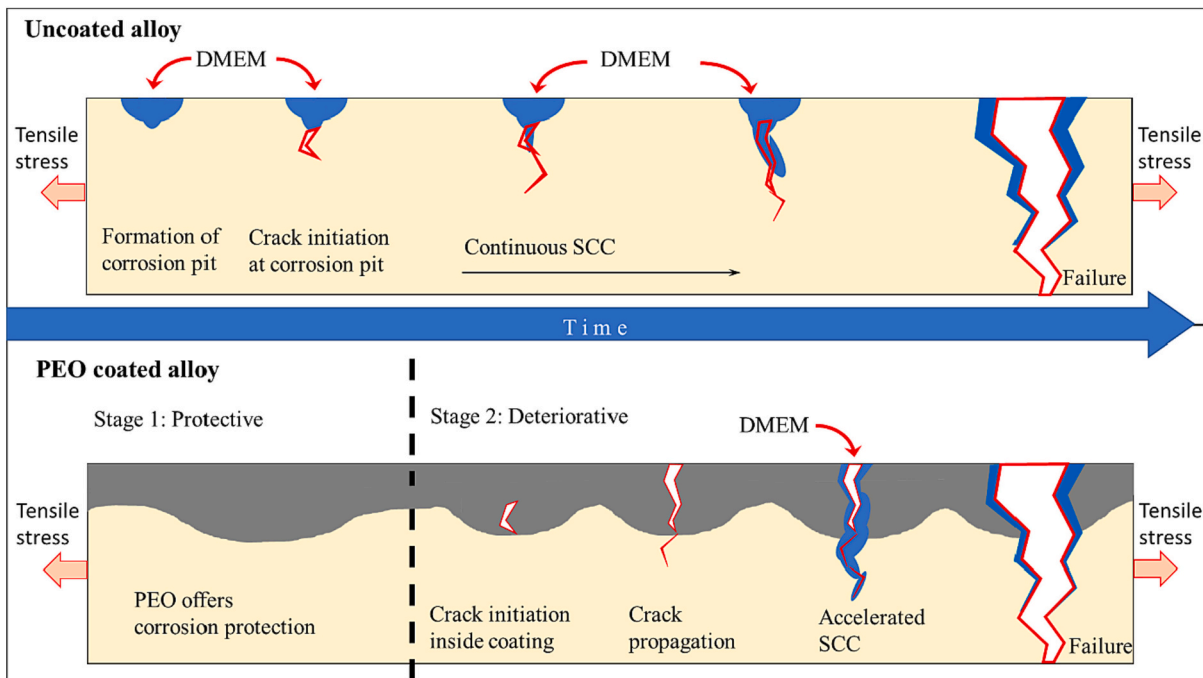
Fig. 9. Schematic of different SCC mechanisms between uncoated and PEO-coated magnesium alloys. Corrosion pits lead to SCC initiation in uncoated specimens at an early experimental stage, while crack formation inside brittle coating is the precursor event of PEO-coated WE43 for SCC. In the second stage, the crack will enable the permeation of the surrounding fluid to the substrate material under high stresses, which results in a faster crack growth compared to that in uncoated WE43.

corrosion at the initial stage of immersion tests, but also leads to a much more homogeneous corrosion front with significantly less deep pits. Therefore, instead of corrosion pits, the crack initiation inside the brittle coating is the precursor event of PEO-coated WE43, which is only initiated at a critical stress level and delayed in comparison with the uncoated alloy. In the second stage, the crack will propagate into the substrate material as well as towards the outside [24]. Consequently, the crack will enable the permeation of the surrounding fluid to the substrate material at an increased stress level, which leads to a faster crack growth compared to that in uncoated WE43. Concludingly, the PEO coating provides protection against SCC in its undamaged state, while the degradation of mechanical integrity of the brittle coating triggers deteriorative effects on the substrate magnesium alloy and accelerates crack growth.

In this context, the experimental results of the residual strength after CLT tests reveal that the critical stress level of 0.8 R_m dramatically accelerates the coupled corrosion and fracture process in both specimen groups. Moreover, the protective effects of the coating at the early stage of SCC are eliminated by the degradation of the mechanical integrity of the brittle coating under the applied CLT conditions.

Adjacent to area A, which encircles the specimens' circumferences, an oxidised region can be identified by its darker appearance in the BSE SEM images (Fig. 7b and Fig. 8b). In both specimens, a significant number of secondary cracks are visible inside areas A and B. Moreover, area B shows V-shaped ridges or chevron markings, which is typical for brittle fractures and implies that the fracture mechanism changes between areas A and B. Following stress corrosion cracking in the circumferential region, a brittle fracture is initiated. In magnesium alloys, the appearance of such brittle fracture morphology in a stress corrosion environment is often associated with hydrogen embrittlement. One underlying mechanism is hydrogen ingress in the region around the crack tip, leading to increased hydrogen concentration in this area, which in turn results in embrittlement and facilitates crack propagation through this embrittled area. Furthermore, the source of hydrogen is of importance for hydrogen-assisted failures. In this context, the coating process increases the atomic hydrogen concentration of the underlying substrate material. Thereby, hydrogen-assisted mechanisms are favoured as critical hydrogen concentrations for crack propagation are reached after shorter times. The initially higher hydrogen concentration of the PEO-coated specimens explains the smoother appearance of fan-shaped ridges as the crack follows an easy path.

The side view of the failed specimens is shown in Fig. 10. In the uncoated specimen, a large number of secondary cracks are present that are aligned perpendicular to the loading direction, which is a common feature of SCC. In the coated specimen, coating damage is shown in terms of aligned microcracks and corrosion products formed on the surface of the coating.

In general, the fracture surfaces of both specimen groups support the phenomenological description of CLT fractures suggested by Raja et al. [18], i.e., a precursor event occurs, the crack initiates and then grows. The crack growth is driven by a hydrogen-assisted mechanism and proceeds slowly at the initial stage. With increasing crack size, the local stress concentrations become sufficiently high, leading to faster crack propagation until final overloading.

4.3. Slow strain rate testing

Fig. 11 presents typical stress-strain curves of non-coated and PEO-

coated WE43 alloy in the SSRT experiments in DMEM medium with three different strain rates (v1, v2, v3). The curves show that the failures occurred in the plastic deformation stage. The elongation-to-failure significantly decreased in DMEM which indicates that the non-coated and coated WE43 alloy suffered significant embrittlement in DMEM. For quantifying the SCC susceptibility of the two tested groups, the resultant sensitivity values of the tensile strength I_{UTS} and the elongation-to-failure I_ε are presented in Fig. 11. The SCC susceptibility index expresses the percentage loss of the property referred to the non-coated alloy tested in air, with higher values indicating higher SCC susceptibility.

The uncoated WE43 alloy reveals an almost strain-rate independent decrease of 12 % in the ultimate tensile strength. In comparison with the results of other magnesium alloys in aggressive environments in Table 3, this I_{UTS} value indicates very good SCC resistance of the WE43 alloy. In contrast, the elongation-to-failure is significantly decreased by the corrosive environment. I_ε is 56 % in the case of the strain rate v1 and takes values about 82 % for v2 and v3, indicating the effect of the decrease in strain rate on more pronounced material embrittlement. The coated specimen group shows similar results, but slightly larger values. However, only the coated specimens show a strain-rate dependent decrease in the material strength, especially in the case of the smallest strain rate v3. The slower strain rate allows more corrosion time for a higher degree of material embrittlement and therefore leads to a smaller elongation to failure.

Uncoated (Fig. 12) and coated (Fig. 13) specimens show similar fracture characteristics observed in the failing specimens in CLT tests. The fracture surface of the uncoated specimen in Fig. 12a reveals a distinct area of stress corrosion cracking along its circumference with a larger number of crack initiation sites that are again marked as region A. The side view of the specimen is presented in Fig. 12d. It is shown that the surface is covered by corrosion products and contains a large number of cracks orientated perpendicular to the loading axis. Fig. 12e shows a typical crack in more detail, revealing corrosion products inside the crack, which clearly indicate stress corrosion cracking. Region A is adjacent by a region of steep radial fan-shaped ridges that are typical features for brittle fracture. A more detailed view of area B in Fig. 12b shows the corrosion-assisted cracking accompanied by a network of
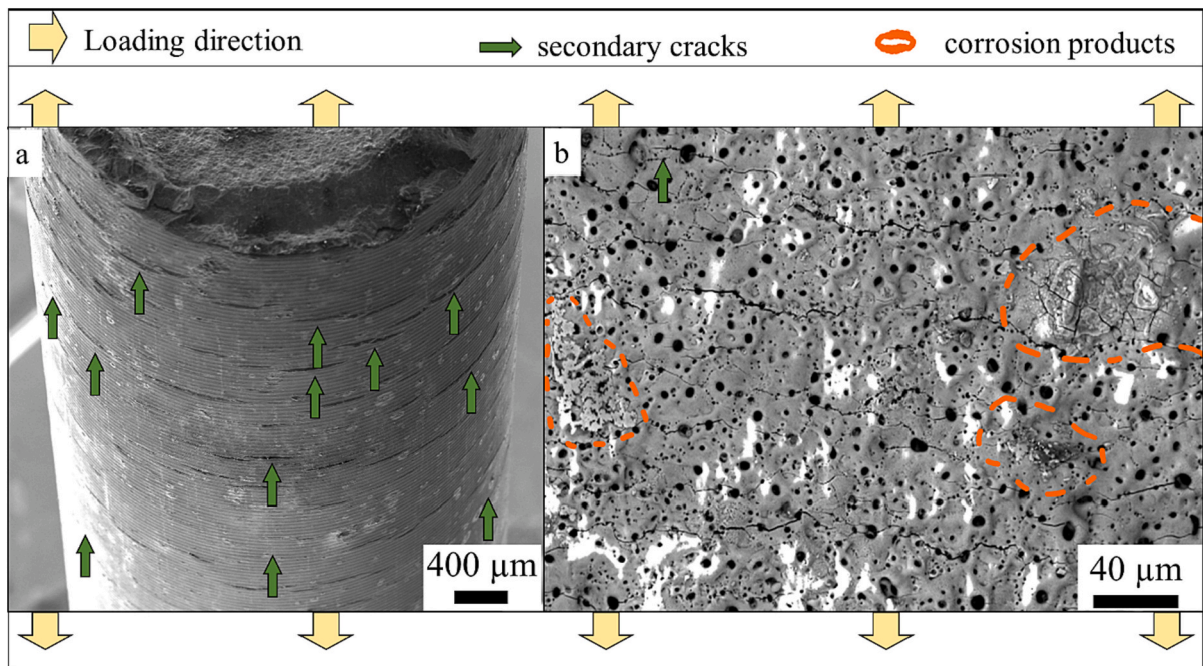
Fig. 10. SEM images of side-view of failed specimens in the 0.8 Rm CLT loading case: (a) Overview of uncoated specimen failing after 7 h showing aligned secondary cracks. (b) The coating surface with aligned secondary microcracks and corrosion products of the coated specimen failed after 9.7 h.
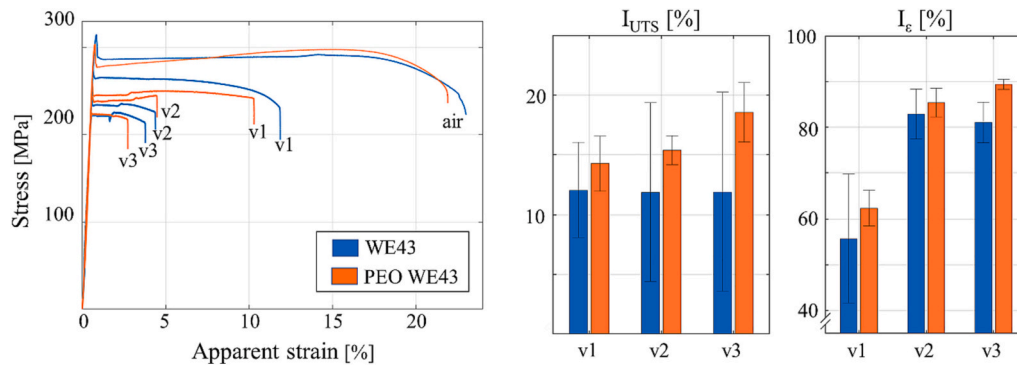
Fig. 11. Typical stress-strain curves of non-coated (blue) and PEO-coated (red) WE43 alloy in the SSRT in DMEM medium with three different strain rates (left), and summary of SSRT susceptibility indices of tensile strength I_{UTS} (centre) and elongation-to-failure I_ε (right).

Table 3
Comparison of SCC susceptibility factors for different magnesium alloys.

Alloy	Fluid	Strain Rate	I_{UTS} [%]	I_ε [%]	Grain size [μm]	Ref.
WE43	DMEM	1.1×10^{-6}	12	56	2.7	
WE43	DMEM	3.6×10^{-7}	12	83	2.7	
WE43	DMEM	2.2×10^{-7}	12	81	2.7	
WE43 + PEO	DMEM	1.1×10^{-6}	14	62	2.7	
WE43 + PEO	DMEM	3.6×10^{-7}	15	85	2.7	
WE43 + PEO	DMEM	2.2×10^{-7}	19	89	2.7	
AZ61	ASTM D1348	1×10^{-6}	33	81	40	[48]
AZ61 + PEO	ASTM D1348	1×10^{-6}	23.4	76	40	[48]
WE43	DMEM	1×10^{-6}	20	32	13	[43]
Mg-Zn-Zr	3.5 wt% NaCl	1×10^{-6}	–	98	5	[49]
ZX50	m-SBF	3.1×10^{-7}	27	82	4	[17]
WZ21	m-SBF	3.1×10^{-7}	31	73	7	[17]
WE43	m-SBF	3.1×10^{-7}	20	53	15	[17]
AZ91D	m-SBF	5×10^{-7}	25	37	–	[50]
Mg3Zn1Ca	m-SBF	5×10^{-7}	42	45	–	[50]
AZ31	Hank's solution	1×10^{-7}	33	82	–	[51]
AZ31+ LSP*	Hank's solution	1×10^{-7}	32	80	–	[51]
AZ31 + PC**	Hank's solution	1×10^{-7}	33	81	–	[51]
AZ31 + LSP*/ PC**	Hank's solution	1×10^{-7}	29	76	–	[51]
AZ31	SBF	3.5×10^{-6}	9	75	24.1	[23]
AZ31 + CC***	SBF	3.5×10^{-6}	7	68	–	[23]
AZ31B	HBSS	1×10^{-4}	53	63	–	[52]
AZ31B + 6 h aged	HBSS	1×10^{-4}	53	61	–	[52]

* LSP = laser shock peening.
** PC = phosphate conversion.
*** CC = cryogenic cooling.

secondary cracks and oxidations along primary cracks. A mixed mode of transgranular and intergranular cracking can be identified, which is consistent with the reported embrittlement behaviour of rare-earth alloys with similar grain sizes [17,49,53]. The intergranular cracking can also be related to the electrochemical dissolution of the precipitates at the grain boundaries, which has also been observed in other studies as hydrogen-assisted embrittlement [17,53,54]. Final failure results from overloading as we observe dimple formation, as shown in Fig. 12c in more detail. During SSRT experiments, the exposure to high stress levels favours hydrogen-assisted mechanisms and thereby leads to brittle failure patterns. Furthermore, it is emphasised that the elongation-to-failures exceeds 10 %, which is very high in comparison to other reported results [21,23,36,42,49,51,52,55], although the sensitivity index of the elongation to failure reveals a detrimental effect of the fluid.

As shown in Fig. 13a, the area of stress corrosion cracking appears smaller in the coated specimen, as it has already been observed in CLT fracture surfaces. Such differences related to the SSC resistance have already been reported in the SSRT of an AZ80 alloy SSRT tested in SBF of various pH values. A thicker region of stress corrosion cracking was attributed to a better SCC resistance as the specimen had a longer time for crack propagation [20]. Therefore, the thicker area A of the uncoated alloy implies that the uncoated alloy has a better SCC resistance, which is also confirmed by the susceptibility values.

Similar to the CLT results, protective/deteriorative effects of the brittle coating on the SCC behaviour of the substrate alloys were observed under SSRT conditions. However, the sensitivity values imply that the protective effect of the coating is lost at a much earlier experimental stage, and its deteriorative impact is more dominant under SSRT conditions. This observation is also confirmed by the side view of the specimen in Fig. 14a and b. It is seen that a large number of aligned secondary cracks penetrate deeply into the substrate material. Compared to the coating damage observed in CLT tests (Fig. 10), the coating damage is much more severe in SSRT tests as deep secondary cracks and partly exfoliation can be identified on the coating surface. This extensive coating damage facilitates fluid permeation to the underlying magnesium alloy and the initiation of SCC. Exfoliation of the coating is not observed in the specimens tested with the lowest strain rate, as shown in Fig. 14c. It might be attributed to the smallest overall elongation-to-failure in the case, which is not sufficiently large for exfoliation of the coating.

5. Conclusions

The present study has investigated the effect of PEO coating on the stress corrosion cracking behaviour of an as-extruded rare-earth magnesium alloy WE43 under different loading conditions. To ensure the required sterile test conditions for applying physiological fluids with organic compounds, a new experimental setup was developed to enable corrosion experiments under mechanical loadings. For quantifying the
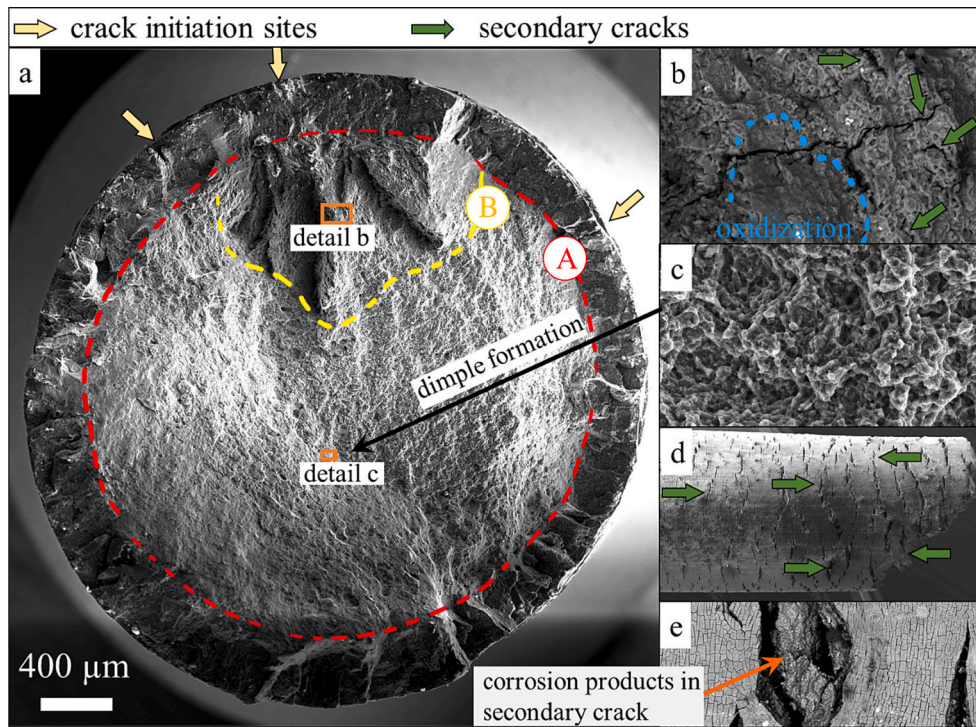
Fig. 12. SEM images of the uncoated specimen in SSRT with the strain rate v1. (a) Overall, the fracture surface reveals a thick and distinct area A of stress corrosion cracking and area B with steep ridges. (b) Higher magnification of detail b inside of the brittle region B shows secondary cracks and oxidised areas. (c) Higher magnified detail c with evidence of dimple formation inside the overload failure region. (d) Side view of fractured specimen shows a large number of aligned secondary cracks. (e) High magnification image reveals corrosion products inside the secondary crack.
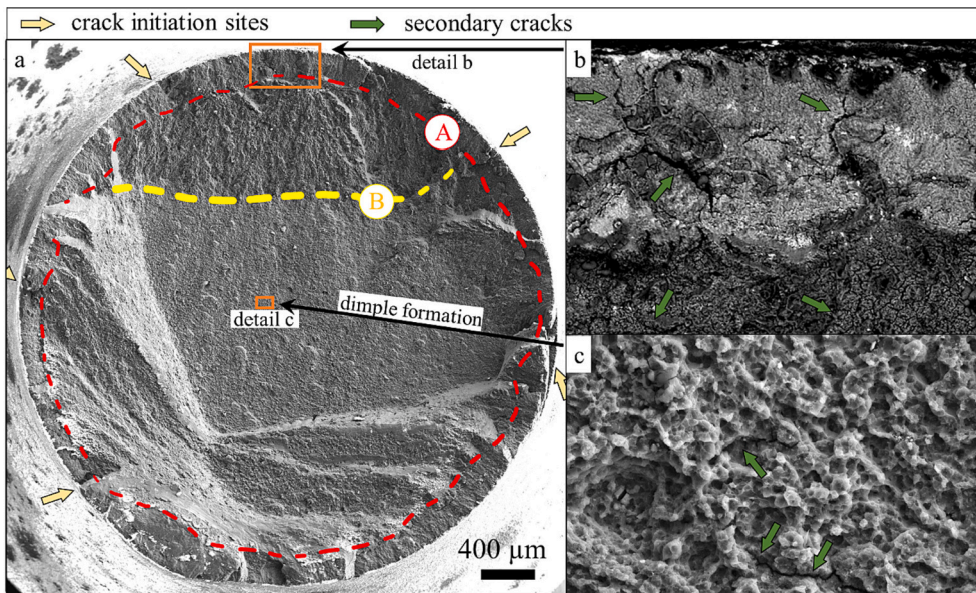
Fig. 13. SEM images of fracture surface of coated specimen in SSRT with the strain rate v1: (a) Overall fracture surface reveals a thinner distinct area A of stress corrosion cracking and the brittle fracture area B with crack coalescence. (b) BSE SEM image at higher magnification of detail b showing secondary cracks and oxidised areas. (c) Higher magnification of detail c with evidence of dimple formation inside the overload failure region.

influence of loading conditions on the SCC behaviour, constant loading tests and slow strain rate tests were performed under in vitro conditions. Moreover, the fracture surfaces of specimens were systematically analysed using scanning electron microscopy to clarify the SCC mechanisms. Based on the experimental results and discussions, the following conclusions can be drawn:

1. CLT tests reveal a critical stress level of 0.8 R_m, leading to the high probability of specimen failure in uncoated and coated specimens.
2. The residual mechanical strength of WE43 after CLT tests with stress levels below the critical value is insensitive to the applied stress level and loading duration ($\leq$ 3 days). The reduction of the tensile strength after 3 days loaded with 0.6 R_m is 3.1 % and 2.2 % for uncoated and PEO-coated WE43, respectively.
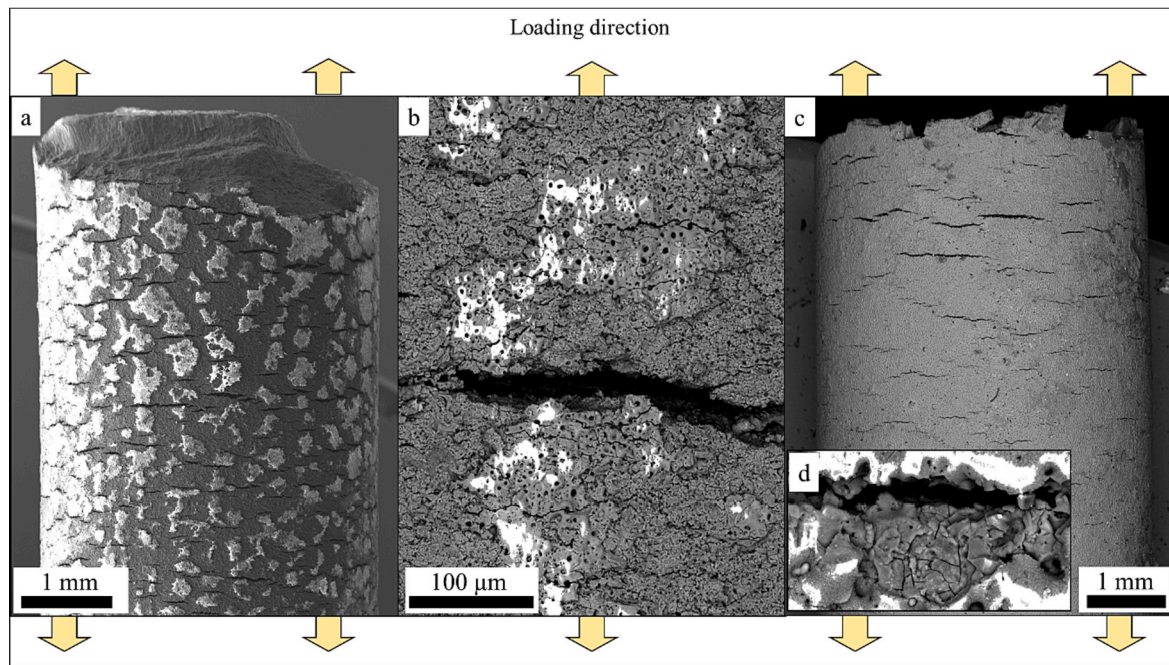
Fig. 14. SEM image of the side view of coated specimen in SSRT with the strain rate v1: (a) Damaged coating shows large aligned secondary cracks that penetrate into the substrate material covered by coating residuals. (b) Higher magnification of large secondary crack in the coating. (c) Side view of the specimen with large and deep aligned secondary cracks. (d) High magnification of secondary cracks shows corrosion products inside of it.

3. Fracture surfaces of uncoated and coated specimens failed in CLT tests reveal distinct patterns of stress corrosion cracking: (1) a circumferential area of stress corrosion cracking; (2) a brittle fracture area with an oxidised region; (3) and a region of final overload failure.

4. Fractographical analysis suggests that the coating protects the substrate material only at the initial stage of corrosion under low stresses. The transition from the protective to a detrimental stage is triggered by crack formation inside the brittle coating, which enables the permeation of the surrounding fluid to the substrate material and leads to faster crack growth than uncoated WE43.

5. Compared with the other magnesium alloys in aggressive environments, the uncoated and PEO-coated WE43 alloys show high SCC resistance in SSRT conditions. The resultant sensitivity factor I_{UTS} of the uncoated specimen is 12 %, while it increases to 19 % in the coated specimens with decreasing strain rate.

6. Both specimen groups suffer strain-rate dependent embrittlement in DMEM in SSRT. The elongation-to-failure is reduced in the uncoated specimen group by 56 % at $1.1 \times 10^{-6}\,s^{-1}$ and by 81 % at $2.2 \times 10^{-7}\,s^{-1}$, and in the coated specimen group by 62 % at $1.1 \times 10^{-6}\,s^{-1}$ and by 89 % at $2.2 \times 10^{-7}\,s^{-1}$, respectively. In SSRT conditions, the deteriorative impact of the coating increases with decreasing strain rate, which results in a strain-rate dependent SCC susceptibility of the coated specimens.

CRediT authorship contribution statement

Julia Nachtsheim: Conceptualization, Data curation, Formal analysis, Investigation, Writing – original draft. **Songyun Ma:** Conceptualization, Funding acquisition, Methodology, Project administration, Supervision, Writing – review & editing. **Jaka Burja:** Investigation, Methodology, Writing – review & editing. **Bernd Markert:** Resources, Supervision, Writing – review & editing.

Declaration of competing interest

The authors declare that they have no known competing financial interests or personal relationships that could have appeared to influence the work reported in this paper.

Data availability

Data will be made available on request.

References

[1] R. Waksman, R. Pakala, P.K. Kuchulakanti, R. Baffour, D. Hellinga, R. Seabron, F. O. Tio, E. Wittchow, S. Hartwig, C. Harder, R. Rohde, B. Heublein, A. Andreae, K. H. Waldmann, A. Haverich, Safety and efficacy of bioabsorbable magnesium alloy stents in porcine coronary arteries, Catheter. Cardiovasc. Interv. 68 (2006) 607–617, https://doi.org/10.1002/ccd.20727.

[2] N.T. Kirkland, N. Birbilis, M.P. Staiger, Assessing the corrosion of biodegradable magnesium implants: a critical review of current methodologies and their limitations, Acta Biomater. 8 (2012) 925–936, https://doi.org/10.1016/j.actbio.2011.11.014.

[3] Y. He, H. Tao, Y. Zhang, Y. Jiang, S. Zhang, C. Zhao, J. Li, B. Zhang, Y. Song, X. Zhang, Biocompatibility of bio-Mg-Zn alloy within bone with heart, liver, kidney and spleen, Chin. Sci. Bull. 54 (2009) 484–491, https://doi.org/10.1007/s11434-009-0080-z.

[4] N. Erdmann, N. Angrisani, J. Reifenrath, A. Lucas, F. Thorey, D. Bormann, A. Meyer-Lindenberg, Biomechanical testing and degradation analysis of MgCa0.8 alloy screws: a comparative in vivo study in rabbits, Acta Biomater. 7 (2011) 1421–1428, https://doi.org/10.1016/j.actbio.2010.10.031.

[5] V. Tsakiris, C. Tardei, F.M. Clicinschi, Biodegradable Mg alloys for orthopedic implants – a review, J. Magn. Alloys 9 (2021) 1884–1905, https://doi.org/10.1016/j.jma.2021.06.024.

[6] D. Raftopoulos, E. Katsamanis, F. Saul, W. Liu, S. Saddernit, Communications An Intermediate Loading Rate Technique for the Determination of Mechanical Properties of Human Femoral Cortical Bone, n.d.

[7] X.N. Gu, Y.F. Zheng, A review on magnesium alloys as biodegradable materials, Front Mater Sci China 4 (n.d.) 111–115. doi:https://doi.org/10.1007/s11706-010 -0024-1.

[8] K.C. Tekin, U. Malayoğlu, S. Shrestha, Electrochemical behavior of plasma electrolytic oxide coatings on rare earth element containing mg alloys, Surf. Coat. Technol. 236 (2013) 540–549, https://doi.org/10.1016/j.surfcoat.2013.10.051.

[9] R. Chaharmahali, A. Fattah-alhosseini, K. Babaei, Surface characterization and corrosion behavior of calcium phosphate (Ca-P) base composite layer on Mg and its alloys using plasma electrolytic oxidation (PEO): a review, J. Magn. Alloys 9 (2021) 21–40, https://doi.org/10.1016/j.jmea.2020.07.004.

[10] Y. Wu, Y.M. Wang, D.W. Zhao, N. Zhang, H. Li, J. Li, Y. Wang, Y. Zhao, J. Yan, Y. Zhou, In vivo study of microarc oxidation coated mg alloy as a substitute for bone defect repairing: degradation behavior, mechanical properties, and bone response, Colloids Surf. B: Biointerfaces 181 (2019) 349–359, https://doi.org/ 10.1016/j.colsurfb.2019.05.052.

[11] C. Rendenbach, H. Fischer, A. Kopp, K. Schmidt-Bleek, H. Kreiker, S. Stumpp, M. Thiele, G. Duda, H. Hanken, B. Beck-Broichsitter, O. Jung, N. Kröger, R. Smeets, M. Heiland, Improved in vivo osseointegration and degradation behavior of PEO surface-modified WE43 magnesium plates and screws after 6 and 12 months, Mater. Sci. Eng. C 129 (2021), https://doi.org/10.1016/j.msec.2021.112380.

[12] N. Winzer, A. Atrens, G. Song, E. Ghali, W. Dietzel, K.U. Kainer, N. Hort, C. Blawert, A critical review of the Stress Corrosion Cracking (SCC) of magnesium alloys, Adv. Eng. Mater. 7 (2005) 659–693, https://doi.org/10.1002/ adem.200500071.

[13] R.K. Singh Raman, S. Jafari, S.E. Harandi, Corrosion fatigue fracture of magnesium alloys in bioimplant applications: a review, Eng. Fract. Mech. 137 (2015) 97–108, https://doi.org/10.1016/j.engfracmech.2014.08.009.

[14] S. Jafari, S.E. Harandi, R.K. Singh Raman, A review of stress-corrosion cracking and corrosion fatigue of magnesium alloys for biodegradable implant applications, JOM 67 (2015) 1143–1153, https://doi.org/10.1007/s11837-015-1366-z.

[15] S. Jafari, R.K. Singh Raman, C.H.J. Davies, Corrosion fatigue of a magnesium alloy in modified simulated body fluid, Eng. Fract. Mech. 137 (2015) 2–11, https://doi. org/10.1016/j.engfracmech.2014.07.007.

[16] S.E. Harandi, P.C. Banerjee, C.D. Easton, R.K. Singh Raman, Influence of bovine serum albumin in Hanks' solution on the corrosion and stress corrosion cracking of a magnesium alloy, Mater. Sci. Eng. C 80 (2017) 335–345, https://doi.org/ 10.1016/j.msec.2017.06.002.

[17] L. Choudhary, R.K. Singh Raman, J. Hofstetter, P.J. Uggowitzer, In-vitro characterization of stress corrosion cracking of aluminium-free magnesium alloys for temporary bio-implant applications, Mater. Sci. Eng. C 42 (2014) 629–636, https://doi.org/10.1016/j.msec.2014.06.018.

[18] V.S. Raja, B.S. Padekar, Role of chlorides on pitting and hydrogen embrittlement of Mg-Mn wrought alloy, Corros. Sci. 75 (2013) 176–183, https://doi.org/10.1016/j. corsci.2013.05.030.

[19] A. Bahmani, M. Lotfpour, M. Taghizadeh, W.J. Kim, Corrosion behavior of severely plastically deformed Mg and Mg alloys, J. Magn. Alloys 10 (2022) 2607–2648, https://doi.org/10.1016/j.jma.2022.09.007.

[20] L. He, J. Yang, Y. Xiong, R. Song, Effect of solution pH on stress corrosion cracking behavior of modified AZ80 magnesium alloy in simulated body fluid, Mater. Chem. Phys. 261 (2021), https://doi.org/10.1016/j.matchemphys.2021.124232.

[21] J. Jiang, Q. Xie, M. Qiang, A. Ma, E.K. Taylor, Y. Li, D. Song, J. Chen, Stress corrosion cracking behaviors of RE-containing ME21 magnesium alloy processed by equal-channel angular pressing, J. Rare Earths 37 (2019) 88–94, https://doi. org/10.1016/j.jre.2018.04.015.

[22] Y. Zhang, J. You, J. Lu, C. Cui, Y. Jiang, X. Ren, Effects of laser shock processing on stress corrosion cracking susceptibility of AZ31B magnesium alloy, Surf. Coat. Technol. 204 (2010) 3947–3953, https://doi.org/10.1016/j.surfcoat.2010.03.015.

[23] M. Peron, R. Bertolini, A. Ghiotti, J. Torgersen, S. Bruschi, F. Berto, Enhancement of stress corrosion cracking of AZ31 magnesium alloy in simulated body fluid thanks to cryogenic machining, J. Mech. Behav. Biomed. Mater. 101 (2020), https://doi.org/10.1016/j.jmbbm.2019.103429.

[24] Y. Zou, Y. Wang, D. Wei, Q. Du, J. Ouyang, D. Jia, Y. Zhou, In-situ SEM analysis of brittle plasma electrolytic oxidation coating bonded to plastic aluminum substrate: microstructure and fracture behaviors, Mater. Charact. 156 (2019), https://doi. org/10.1016/j.matchar.2019.109851.

[25] P. Bala Srinivasan, C. Blawert, W. Dietzel, Effect of plasma electrolytic oxidation treatment on the corrosion and stress corrosion cracking behaviour of AM50 magnesium alloy, Mater. Sci. Eng. A 494 (2008) 401–406, https://doi.org/ 10.1016/j.msea.2008.04.031.

[26] Y. Xiong, Y. Shen, L. He, Z. Yang, R. Song, Stress corrosion cracking behavior of LSP/MAO treated magnesium alloy during SSRT in a simulated body fluid, J. Alloys Compd. 822 (2020), https://doi.org/10.1016/j.jallcom.2020.153707.

[27] M.C. Zhao, M. Liu, G.L. Song, A. Atrens, Influence of pH and chloride ion concentration on the corrosion of Mg alloy ZE41, Corros. Sci. 50 (2008) 3168–3178, https://doi.org/10.1016/j.corsci.2008.08.023.

[28] Y. Xin, K. Huo, H. Tao, G. Tang, P.K. Chu, Influence of aggressive ions on the degradation behavior of biomedical magnesium alloy in physiological environment, Acta Biomater. 4 (2008) 2008–2015, https://doi.org/10.1016/j. actbio.2008.05.014.

[29] R.C. Zeng, Y. Hu, S.K. Guan, H.Z. Cui, E.H. Han, Corrosion of magnesium alloy AZ31: the influence of bicarbonate, sulphate, hydrogen phosphate and dihydrogen phosphate ions in saline solution, Corros. Sci. 86 (2014) 171–182, https://doi.org/ 10.1016/j.corsci.2014.05.006.

[30] W. Ma, Y. Liu, W. Wang, Y. Zhang, Effects of electrolyte component in simulated body fluid on the corrosion behavior and mechanical integrity of magnesium, Corros. Sci. 98 (2015) 201–210, https://doi.org/10.1016/j.corsci.2015.05.012.

[31] S. Johnston, M. Dargusch, A. Atrens, Building towards a standardised approach to biocorrosion studies: a review of factors influencing Mg corrosion in vitro pertinent to in vivo corrosion, Sci. China Mater. 61 (2018) 475–500, https://doi.org/ 10.1007/s40843-017-9173-7.

[32] T. Kokubo, H. Takadama, How useful is SBF in predicting in vivo bone bioactivity? Biomaterials 27 (2006) 2907–2915, https://doi.org/10.1016/j. biomaterials.2006.01.017.

[33] A. Yamamoto, S. Hiromoto, Effect of inorganic salts, amino acids and proteins on the degradation of pure magnesium in vitro, Mater. Sci. Eng. C 29 (2009) 1559–1568, https://doi.org/10.1016/j.msec.2008.12.015.

[34] D. Mei, S.V. Lamaka, X. Lu, M.L. Zheludkevich, Selecting medium for corrosion testing of bioabsorbable magnesium and other metals – a critical review, Corros. Sci. 171 (2020), https://doi.org/10.1016/j.corsci.2020.108722.

[35] L. Chen, C. Blawert, J. Yang, R. Hou, X. Wang, M.L. Zheludkevich, W. Li, The stress corrosion cracking behaviour of biomedical Mg-1Zn alloy in synthetic or natural biological media, Corros. Sci. 175 (2020), https://doi.org/10.1016/j. corsci.2020.108876.

[36] S.E. Harandi, P.C. Banerjee, C.D. Easton, R.K. Singh Raman, Influence of bovine serum albumin in Hanks' solution on the corrosion and stress corrosion cracking of a magnesium alloy, Mater. Sci. Eng. C 80 (2017) 335–345, https://doi.org/ 10.1016/j.msec.2017.06.002.

[37] J. Liu, B. Liu, S. Min, B. Yin, B. Peng, Z. Yu, C. Wang, X. Ma, P. Wen, Y. Tian, Y. Zheng, Biodegradable magnesium alloy WE43 porous scaffolds fabricated by laser powder bed fusion for orthopedic applications: process optimization, in vitro and in vivo investigation, Bioact. Mater. 16 (2022) 301–319, https://doi.org/ 10.1016/j.bioactmat.2022.02.020.

[38] P.D. Darbre, F. Mannello, C. Exley, Aluminium and breast cancer: sources of exposure, tissue measurements and mechanisms of toxicological actions on breast biology, J. Inorg. Biochem. 128 (2013) 257–261, https://doi.org/10.1016/j. jinorgbio.2013.07.005.

[39] M. Dey, R.K. Singh, Neurotoxic effects of aluminium exposure as a potential risk factor for Alzheimer's disease, Pharmacol. Rep. 74 (2022) 439–450, https://doi. org/10.1007/s43440-022-00353-4.

[40] J. Nachtsheim, S. Ma, J. Burja, B.Š. Batič, B. Markert, Tuning the long-term corrosion behaviour of biodegradable WE43 magnesium alloy by PEO coating, Surf. Coat. Technol. 474 (2023) 130115, https://doi.org/10.1016/j. surfcoat.2023.130115.

[41] J. Nachtsheim, J. Burja, S. Ma, B. Markert, Long-term in vitro corrosion of biodegradable WE43 magnesium alloy in DMEM, Metals (Basel). 12 (2022), https://doi.org/10.3390/met12122062.

[42] L. Chen, Y. Sheng, H. Zhou, Z. Li, X. Wang, W. Li, Influence of a MAO+PLGA coating on biocorrosion and stress corrosion cracking behavior of a magnesium alloy in a physiological environment, Corros. Sci. 148 (2019) 134–143, https://doi. org/10.1016/j.corsci.2018.12.005.

[43] B. Wang, W. Gao, C. Pan, D. Liu, X. Sun, Effect of the combination of torsional and tensile stress on corrosion behaviors of biodegradable WE43 alloy in simulated body fluid, J. Funct. Biomater. 14 (2023), https://doi.org/10.3390/jfb14020071.

[44] P. Li, Z. Yang, B. He, N. Wang, Y. Chen, Q. Zhao, Y. Zhang, Y. Zhao, Effect of local 'over-growth' on fracture behaviors of coated titanium fiber fabricated by plasma electrolytic oxidation, Surf. Interfaces 36 (2023), https://doi.org/10.1016/ j.surfin.2023.102645.

[45] S. Jafari, R.K.S. Raman, C.H.J. Davies, Stress corrosion cracking of an extruded magnesium alloy (ZK21) in a simulated body fluid, Eng. Fract. Mech. 201 (2018) 47–55, https://doi.org/10.1016/j.engfracmech.2018.09.002.

[46] L. Chen, C.M. Tseng, Y. Qiu, J. Yang, C.L. Chang, X. Wang, W. Li, A layer-by-layer assembled coating for improved stress corrosion cracking on biomedical magnesium alloy in cell culture medium, Surf. Coat. Technol. 403 (2020), https:// doi.org/10.1016/j.surfcoat.2020.126427.

[47] K. van Gaalen, C. Quinn, M. Weiler, F. Gremse, F. Benn, P.E. McHugh, T. J. Vaughan, A. Kopp, Predicting localised corrosion and mechanical performance of a PEO surface modified rare earth magnesium alloy for implant use through in-silico modelling, Bioact. Mater. 26 (2023) 437–451, https://doi.org/10.1016/j. bioactmat.2023.03.009.

[48] P. Bala Srinivasan, R. Zettler, C. Blawert, W. Dietzel, A study on the effect of plasma electrolytic oxidation on the stress corrosion cracking behaviour of a wrought AZ61 magnesium alloy and its friction stir weldment, Mater. Charact. 60 (2009) 389–396, https://doi.org/10.1016/j.matchar.2008.10.010.

[49] B.J. Wang, D.K. Xu, J. Sun, E.H. Han, Effect of grain structure on the stress corrosion cracking (SCC) behavior of an as-extruded Mg-Zn-Zr alloy, Corros. Sci. 157 (2019) 347–356, https://doi.org/10.1016/j.corsci.2019.06.017.

[50] L. Choudhary, R.K. Singh Raman, Mechanical integrity of magnesium alloys in a physiological environment: slow strain rate testing based study, Eng. Fract. Mech. 103 (2013) 94–102, https://doi.org/10.1016/j.engfracmech.2012.09.016.

[51] H. Liu, J. Gu, Z. Tong, D. Yang, H. Yang, X. Ren, Improving stress corrosion cracking resistance of AZ31 magnesium alloy in Hanks' solution via phosphate conversion with laser shock peening pretreatment, Mater. Today Commun. 31 (2022), https://doi.org/10.1016/j.mtcomm.2022.103678.

[52] S.T. Vagge, S. Bakshi, Effect of precipitation hardening on stress corrosion cracking susceptibility index of AZ31B magnesium alloy in simulated body fluid, in: Mater Today Proc, Elsevier Ltd, 2020, pp. 2191–2199, https://doi.org/10.1016/j. matpr.2020.05.568.

[53] M. Bobby Kannan, W. Dietzel, C. Blawert, A. Atrens, P. Lyon, Stress corrosion cracking of rare-earth containing magnesium alloys ZE41, QE22 and Elektron 21

(EV31A) compared with AZ80, Mater. Sci. Eng. A 480 (2008) 529–539, https://doi.org/10.1016/j.msea.2007.07.070.

[54] R. Arrabal, E. Matykina, F. Viejo, P. Skeldon, G.E. Thompson, Corrosion resistance of WE43 and AZ91D magnesium alloys with phosphate PEO coatings, Corros. Sci. 50 (2008) 1744–1752, https://doi.org/10.1016/j.corsci.2008.03.002.

[55] D. Dubey, K. Kadali, S.S. Panda, A. Kumar, J. Jain, K. Mondal, S.S. Singh, Comparative study on the stress corrosion cracking susceptibility of AZ80 and AZ31 magnesium alloys, Mater. Sci. Eng. A 792 (2020), https://doi.org/10.1016/j.msea.2020.139793.